JOURNAL OF THERMOPHYSICS AND HEAT TRANSFER
Vol. 20, No. 4, October–December 2006

Uncertainty Analysis of Laminar Aeroheating Predictions for Mars Entries

Deepak Bose*
Eloret Corporation, NASA Ames Research Center, Moffett Field, California 94035
Michael J. Wright†
NASA Ames Research Center, Moffett Field, California 94035
and
Grant E. Palmer‡
Eloret Corporation, NASA Ames Research Center, Moffett Field, California 94035

A Monte Carlo sensitivity and uncertainty analysis is performed for a laminar convective heating prediction in a moderate Mars atmospheric entry condition using a nonequilibrium reacting Navier–Stokes computational fluid dynamics code. The objectives are to isolate the rate limiting mechanisms and identify the chief sources of aeroheating uncertainty. A flux-based wall catalysis formulation is developed and used to define four different catalytic regimes that are then individually analyzed at three different trajectory points. A total of 130 input parameters are statistically varied to short list a handful of parameters that essentially control the heat flux prediction. The uncertainties in these key input parameters are estimated, and a full Monte Carlo uncertainty analysis is performed. The results obtained provide the quantitative contribution of uncertainties in key modeling parameters, such as collision integrals, wall catalysis, and reaction rates to the final heat flux uncertainty. It is found that in high and low catalytic regimes, the collision integrals (which govern the transport properties of the mixture) contribute a large portion of the uncertainty, whereas in the moderately catalytic regime the catalytic properties of the surface contribute almost all of the uncertainty.

Nomenclature

A	=	rate constant
D	=	dissociation energy, K
E	=	energy, eV
h	=	enthalpy, J/kg
k	=	Arrhenius rate
M	=	molecular weight, kg/kmol
n	=	number density, cm^{-3}
p_2	=	preference factor, Eq. (6)
q	=	heat transfer, W/cm^2
R	=	gas constant
T	=	temperature, K
t	=	time, s
u	=	thermal speed, m/s
V	=	velocity, km/s
Γ	=	particle flux, 1/s
γ	=	reaction probability
κ	=	thermal conductivity
v	=	diffusion velocity, m/s
ρ	=	gas density, kg/m^3
Ω^{11}	=	diffusion collision integral, Å^2
Ω^{22}	=	viscosity collision integral, Å^2

Subscripts

a	=	average
cat	=	catalytic
max	=	maximum
s	=	species
v	=	vibrational
w	=	wall

Superscripts

η	=	preexponential factor
$+$	=	incoming

I. Introduction

NASA'S Mars Technology Program is actively pursuing development and selection of technologies for several proposed Mars exploration missions scheduled to launch during the next several years. NASA's new vision for space exploration also calls for robotic exploration of Mars to lay the groundwork for possible human expeditions. In addition, the NASA In-Space Propulsion Program is considering aerocapture missions to Mars (among several possible destinations) as a means to reduce the onboard propellant requirement (and resulting system mass) for orbital insertion of an arriving vehicle.[1] An aerocapture vehicle is subjected to aerothermal heating as it dissipates the vehicle kinetic energy at the destination planet using atmospheric drag. The performance of this technology is determined by the propellant mass savings as compared to the mass of the aeroshell, which consists of the thermal protection system (TPS) and the underlying substructure. For both aerocapture and direct entry, the selection of an appropriate TPS material, as well as the required thickness (mass) of the TPS for each mission, are determined by the aerothermal environment encountered by the vehicle during the entry. Clearly, aeroheating predictions and their associated uncertainties for Mars entries will be necessary for design and development of TPSs for a variety of missions.

Many investigators have performed aerothermal analysis of Mars entry environments using state-of-the-art computational fluid dynamics (CFD) codes.[2–4] Although CFD simulations provide aeroheating predictions with a greater level of fidelity than simple

Presented as Paper 2005-4682 at the AIAA 38th Thermophysics Conference, Toronto, Canada, 6–9 June 2005; received 8 November 2005; revision received 31 January 2006; accepted for publication 31 January 2006.

*Senior Research Scientist, MS 230-3, Reacting Flow Environments Branch. Member AIAA.
†Senior Research Scientist, MS 230-2, Reacting Flow Environments Branch. Senior Member AIAA.
‡Senior Research Scientist, MS 230-2, Reacting Flow Environments Branch. Associate Fellow AIAA.

engineering correlations, the confidence level associated with these predictions remains largely unknown, especially in the regimes where validation with ground-test or flight data has not been possible. It is well known that aeroheating predictions made from these CFD analyses are sensitive to the physical, chemical, and numerical models employed. The uncertainty in these predictions, which is a critical element of the overall entry system risk, is the result of a combined effect of parametric and structural uncertainties in the underlying models. Parametric uncertainties are due to imprecise measurements or estimates of input parameters, such as reaction rates, thermal relaxation times, transport properties, and wall catalycity. Structural uncertainties, on the other hand, are caused by deficiencies in the formulation of the physical and numerical models intended to represent the true environment. Although prior aerothermal investigations recognize these uncertainties, there have been few rigorous attempts to quantify them and assess their effect on the final aeroheating uncertainty. For the purposes of design and system risk assessment, the uncertainty limits associated with an aeroheating prediction are almost as important as the aeroheating value itself, especially when the limits are large. Without a formal uncertainty analysis, the subsystem risk estimate remains crude, which may result in misplaced priorities in the overall system risk reduction strategy.

In this work, we carry out a systematic Monte Carlo uncertainty and sensitivity analysis for Mars entry aerothermodynamics at moderate entry conditions. A similar uncertainty analysis was performed recently for a Titan entry vehicle to ascertain the uncertainty associated with radiative heating at the stagnation point.[5] The current work will focus on nonablating, laminar convective heating rates on the forebody of a rigid aeroshell. Apart from quantifying the uncertainty in the aeroheating predictions, this technique will allow us to isolate the chief sources of uncertainty in the models. These uncertainty drivers can then be prioritized and targeted for further ground-based investigation or proposed flight instrumentation to maximize return from research. A sensitivity analysis, which is a byproduct of the uncertainty analysis, will also provide valuable insights by identifying the rate-limiting steps and dominant mechanisms, including any nonlinearities or interference effects that would not be seen in a linear analysis. The results of this sensitivity analysis can also be used to identify potential structural uncertainties in the current aeroheating models; if the models employed are correct the sensitivities predicted should be reproducible via targeted experiments.

Among the physical phenomena that play a critical role in the laminar heating rates in the absence of shock-layer radiation and TPS ablation are wall catalysis, boundary-layer transport, and chemical kinetics. Each of these phenomena will be explored in this work. Numerical uncertainties due to grid resolution, choice of flux discretization, etc., are not included. The rest of this paper describes the baseline model and the entry conditions used, followed by a sensitivity analysis to identify a key set of input parameters. This is followed by an estimate of uncertainties that exist in these key parameters at three points along the entry trajectory of the Mars Pathfinder entry vehicle. Finally, we perform a Monte Carlo uncertainty analysis to track the impact of these uncertainties on forebody heat flux.

II. Baseline Conditions and Model

A. Mars Pathfinder Entry Conditions

The primary focus of the analysis in this work will be the Mars Pathfinder entry vehicle, which entered the atmosphere of Mars on 4 July 1997 at a relative velocity of 7.5 km/s (Ref. 6). The forebody of the Pathfinder entry vehicle was a 70.2-deg axisymmetric sphere–cone with a rounded shoulder as shown in Fig. 1. Mars Pathfinder is a good test case because it was a ballistic (nonlifting) entry at a velocity for which convective heating was large but radiative heating was small. The analysis in this paper will be performed at three points on the entry trajectory,[4] summarized in Table 1. However, much of the analysis will concentrate on the peak heating point, for which preflight calculations,[4] assuming a fully catalytic surface, predicted a peak convective heat flux of approximately 110 W/cm^2. A postflight analysis of temperature sensor data concluded that at the stagnation point the temperature data are consistent with a peak heat flux during entry of about 85% of the predicted fully catalytic laminar heating.[4]

Table 1 Trajectory points selected for analysis

t, s	ρ, kg/m^3	V, km/s	T, K	q, W/cm^2
45	2.1×10^{-5}	7.47	112	40
66[a]	2.8×10^{-4}	6.60	169	115
76	6.7×10^{-4}	5.33	170	75

[a]Peak heating.

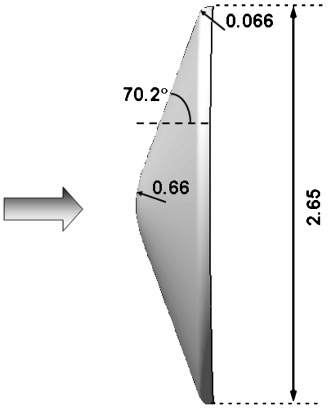

Fig. 1 Mars Pathfinder aeroshell.

B. Numerical and Physical Models

The flowfield computations in this work are performed using the CFD code DPLR.[7] DPLR is a parallel multiblock finite volume code that solves the Navier–Stokes equations including finite rate chemistry and the effects of thermal nonequilibrium. DPLR, along with LAURA,[8] are the primary tools currently used within NASA for aerothermal analysis of Earth and planetary entry vehicles. In addition to the conservation equations for mass and momentum, two energy equations are solved: a total energy equation and a combined vibroelectronic energy equation. In this formulation, it is assumed that the vibrational and electronic modes of the gas are in equilibrium with each other, but not with the translational–rotational component. The energy exchange between the translational–rotational and vibrational–electronic modes is modeled using a Landau–Teller formulation assuming simple harmonic oscillators. Vibrational relaxation times are obtained from Millikan and White[9] for most species. Data by Camac[10] are used for the vibrational relaxation times of CO_2 and CO. Characteristic vibrational temperatures and degeneracies for the simple harmonic oscillator approximation are taken from Gurvich et al.[11]

Viscosity and thermal conductivity are modeled using the species expressions and mixing rules presented by Gupta et al.,[12] which have been shown to be reasonable approximations of the more accurate Chapman–Enskog relations (see Refs. 13 and 14). The self-consistent effective binary diffusion method[15] is used to compute the species diffusion coefficients. This method allows for the variations in species diffusion coefficients to be accurately modeled without sacrificing the requirement that the diffusion velocities sum identically to zero. Required collision integrals are taken from the recent reviews by Wright et al.[16,17] for all binary interactions in the mixture.

C. Chemical Kinetics Model

The Martian atmosphere consists of approximately 97% CO_2 and 3% N_2 by volume, with trace amounts of other species (primarily Ar). A review of the nonequilibrium kinetics of a shock heated mixture of CO_2–N_2 was first presented by Park et al.[18] for an 18-species mixture (CO_2, NCO, CO, CO^+, CN, NO, NO^+, N_2, O_2, O_2^+, C_2, N, N^+, C, C^+, O, O^+, and e) with ionization. Mitcheltree and Gnoffo[3] subsequently presented a reduced eight-species (CO_2, CO, NO, N_2, O_2, N, C, and O) mechanism that neglected ionization. The reactions included in these mechanisms are listed in Table 2. The rates of

Table 2 Reaction mechanisms for Mars entry shock layer

Reaction number	Chemical reactions	Park,[18] 18 species	Mitcheltree and Gnoffo,[3] 8 species
1	$CO_2 + M \Leftrightarrow CO + O + M$	×	×
2	$CO + M \Leftrightarrow C + O + M$	×	×
3	$N_2 + M \Leftrightarrow 2N + M$	×	×
4	$O_2 + M \Leftrightarrow 2O + M$	×	×
5	$NO + M \Leftrightarrow N + O + M$	×	×
6	$C_2 + M \Leftrightarrow 2C + M$	×	——
7	$CN + M \Leftrightarrow C + N + M$	×	——
8	$NCO + M \Leftrightarrow CO + N + M$	×	——
9	$C + e \Leftrightarrow C^+ + 2e$	×	——
10	$O + e \Leftrightarrow O^+ + 2e$	×	——
11	$NO + O \Leftrightarrow O_2 + N$	×	×
12	$N_2 + O \Leftrightarrow NO + N$	×	×
13	$CO + O \Leftrightarrow O_2 + C$	×	×
14	$CO + C \Leftrightarrow C_2 + O$	×	——
15	$CO + N \Leftrightarrow CN + O$	×	——
16	$CO + N \Leftrightarrow NO + C$	——	×
17	$N_2 + C \Leftrightarrow CN + N$	×	——
18	$CN + O \Leftrightarrow NO + C$	×	——
19	$CN + C \Leftrightarrow C_2 + N$	×	——
20	$CO_2 + O \Leftrightarrow O_2 + CO$	×	×
21	$CN + O_2 \Leftrightarrow NCO + O$	×	——
22	$CN + CO_2 \Leftrightarrow NCO + CO$	×	——
23	$CN + NO \Leftrightarrow NCO + N$	×	——
24	$CO + NO \Leftrightarrow NCO + O$	×	——
25	$CO + NO \Leftrightarrow CO_2 + N$	——	×
26	$CO + CO \Leftrightarrow CO_2 + C$	——	×
27	$CN + CO \Leftrightarrow NCO + C$	×	——
28	$N + O \Leftrightarrow NO^+ + e$	×	——
29	$O + O \Leftrightarrow {O_2}^+ + e$	×	——
30	$C + O \Leftrightarrow CO^+ + e$	×	——
31	$NO^+ + C \Leftrightarrow NO + C^+$	×	——
32	${O_2}^+ + O \Leftrightarrow O^+ + O_2$	×	——
33	$NO^+ + N \Leftrightarrow O^+ + N_2$	×	——
34	$NO^+ + O \Leftrightarrow O_2^+ + N$	×	——
35	$CO + C^+ \Leftrightarrow CO^+ + C$	×	——
36	$O_2 + C^+ \Leftrightarrow O_2^+ + C$	×	——

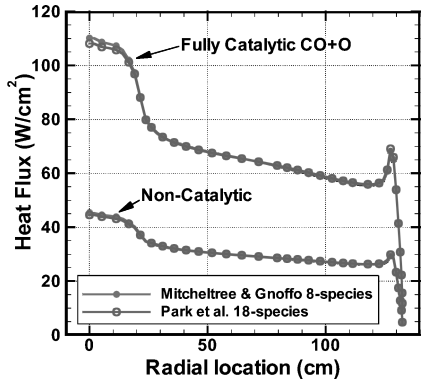

Fig. 2 Laminar convective heat flux on forebody at baseline conditions; effect of different chemical kinetics models in heat flux is shown for both noncatalytic and fully catalytic wall.

the common reactions are taken from Park et al.[18] At the conditions of interest in the present paper the level of ionization in the flowfield is extremely small. Therefore, it is expected that the heat flux computed using the Mitcheltree and Gnoffo eight-species model should be an accurate representation of the flowfield. To test the validity of this assumption, a calculation was performed using each model at the trajectory point discussed earlier for fully catalytic and noncatalytic conditions. Figure 2 shows that the convective heating rates predicted by the two kinetic models are nearly identical, with a maximum difference of 1.8% at the stagnation point for the fully catalytic condition. Based on this result, the eight-species model is used for all cases presented in this paper.

Note that the rates of many of these reactions have not been directly measured at conditions relevant to Martian entry. Some are estimated from indirect observations, whereas others are pure estimates,[18] which make them potentially significant sources of uncertainty. The uncertainties in the relevant reaction rates will be discussed in a later section.

D. Catalysis Model

In the absence of shock-layer radiation, the total incident heat flux to the surface is given by

$$q_w = \left(\kappa \nabla T + \kappa_v \nabla T_v + \sum_{ns} \rho_s h_s v_s \right)_w \tag{1}$$

where the first two terms are the total and vibrational energy conduction and the third term is a result of the recombination of atoms and radicals due to the catalytic activity of the wall. It is well known that the catalytic component of Eq. (1) is a primary source of convective heating for many reentry applications. However, the mechanism involved in the catalytic recombination is poorly understood, in part due to difficulties in performing surface diagnostics at appropriate temperature and pressure. In addition, the surface condition of the TPS material due to past history and exposure to other adsorbing species also alters the catalytic properties, making it further difficult to quantify and address flight traceability issues. Consequently, modeling of catalytic reactions at the surface has been relatively primitive. In fact, for Mars entries, the so-called supercatalytic wall model is frequently employed,[19] in which the gas composition at the surface is specified to be equal to that in the freestream. This model, although it provides a conservative estimate of the heating rate, only accounts for limiting of the recombination processes by diffusion transport of participating species through the boundary layer to the surface. For Mars entries, this boundary condition is especially suspect because it requires the formation of CO_2 via surface reactions at conditions for which no such reaction mechanism is known to exist. The catalytic models are incorporated in the CFD via boundary conditions that are applied to the species mass conservation equations.

In general, surface catalytic reaction models solve a surface site balance equation coupled with gas-phase densities. However, these models assume a heterogeneous reaction model, such as the Langmuir–Hinshelwood (LH) or Eley–Rideal (ER) mechanisms. In the LH model, the participating recombining species are first adsorbed on the surface before recombining and desorbing into the gas phase, whereas in the ER mechanism a gas-phase species recombines directly with an adsorbed species. Several simulations of Mars entry aerothermodynamics have assumed an ER mechanism to describe wall catalysis because of its simplicity. For example, in the Mitcheltree and Gnoffo wall catalysis model[3] $CO + O$ recombination is assumed to occur on the surface via a two-step ER process.

However, the literature indicates that the LH mechanism is more commonly observed than the ER mechanism (see Ref. 20). In fact, direct experimental evidence of the ER mechanism under any condition is lacking. For the well-studied catalytic reaction of CO oxidation on transition metal surfaces, especially the platinum group metals, the LH mechanism is observed to occur. The LH mechanism is also found to govern other catalytic reactions such as CO hydrogenation on metallic surfaces.[20] Therefore, the use of the ER mechanism to describe surface catalysis adds uncertainty that is difficult to assess, especially because experiments measuring catalytic properties of ablative materials in a dissociated Mars environment have never been performed under reentry conditions.

For this work we use a simplified flux-based surface species recombination model that does not rely on a specific heterogeneous reaction model such as the LH or ER mechanism. We know that, for Mars entry, at the conditions of interest, the freestream CO_2 is almost completely dissociated into CO and O, whereas most of the CO formed remains undissociated. Therefore, the composition at the boundary-layer edge consists primarily of CO and O, with the possibility of additional species appearing via recombination. At the conditions of interest in this paper, the trace amounts of N_2 in the atmosphere remain essentially undissociated. Among the several recombination reactions possible at the wall, the following two

involving the dominant species have been proposed[3,4,21] as the reactions that are likely to control the catalytic heating of the vehicle:

Reaction 1: $CO + O \xrightarrow{\gamma_1} CO_2$, $\Delta E = 5.51$ eV.

Reaction 2: $O + O \xrightarrow{\gamma_2} O_2$, $\Delta E = 5.16$ eV.

Other recombination reactions are also possible, but due to their low reactant densities in the boundary layer the resulting effect on catalytic heating will be small. The parameters γ_1 and γ_2 are the reaction probabilities for reactions 1 and 2. However, these parameters do not vary independently because both reactions consume O atoms. From kinetic theory, the incoming flux at the wall for a given species s with number density n_s is written as

$$\Gamma_s^+ = n_s u_s \tag{2}$$

where u_s is one-quarter of the thermal speed of the species $[u_s = (R_s T/2\pi M_s)^{1/2}]$. If γ_O is assumed to be the fraction of O atoms that are lost via either reaction 1 or 2 after they strike the surface, the net O atom flux at the wall is written as

$$\Gamma_O = \gamma_O n_O u_O \tag{3}$$

Let us first consider the case when reaction 1 is CO flux limited, that is, $n_{CO}u_{CO} < n_O u_O$. For this case, the O atom flux at the wall is the sum of the contributions of reactions 1 and 2,

$$\Gamma_O = \gamma_1 n_{CO} u_{CO} + \gamma_2 n_O u_O \tag{4}$$

From Eqs. (3) and (4), we can write γ_O as

$$\gamma_O = \gamma_1 \frac{n_{CO}u_{CO}}{n_O u_O} + \gamma_2 \tag{5}$$

We now define a preference factor for O + O recombination as

$$p_2 = \gamma_2/\gamma_O \tag{6}$$

The preference factor represents the ratio of the flux of O atoms consumed by O + O recombination to the total flux of O atoms consumed by either process. For a given value of p_2, the maximum consumption of O atoms is limited by the CO density, and is given by

$$\gamma_{O,\max} = \min\left[\frac{1}{1-p_2}\left(\frac{n_{CO}u_{CO}}{n_O u_O}\right), 1\right] \tag{7}$$

We further define a catalytic parameter γ_{cat} as the ratio of actual to the maximum possible O atom consumption. Therefore,

$$\gamma_{cat} = \gamma_O/\gamma_{O,\max} \tag{8}$$

Next, we consider the case when reaction 2 is O flux limited, that is, $n_O u_O < n_{CO}u_{CO}$. We note that in this case $\gamma_{O,\max}$ is always one. The sum of the contributions of both reactions to O atom flux is written as

$$\Gamma_O = \gamma_1 n_O u_O + \gamma_2 n_O u_O, \qquad \gamma_O = \gamma_1 + \gamma_2 \tag{9}$$

In each case the value of γ_{cat} can vary between zero (corresponding to a noncatalytic wall from which all O atoms are reflected) and one (corresponding to a fully catalytic wall at which maximum possible O atoms recombine via reactions 1 and 2). It is also evident that because there are two competing reactions consuming O atoms, the catalytic heating will depend on the relative preference of one channel over the other due to their different stoichiometric requirements. The difference in the heats of formation between reactions 1 and 2 is only about 6%, but a strong preference for O_2 recombination will result in lower heating because CO will remain at the wall. We also note that the preference factor p_2, which determines the fraction of recombining O atoms that result in O_2 formation (reaction 2), also varies between zero and one. When the parameters γ_{cat} and p_2 are varied independently between zero and one, the entire window of catalycity can, therefore, be spanned. For example, setting $\gamma_{cat} = 0$ results in a noncatalytic surface regardless of the value of p_2. The fully catalytic limit of the Mitcheltree and Gnoffo model can be reproduced by setting $\gamma_{cat} = 1$ and $p_2 = 0$. In contrast, γ_1 and γ_2 cannot be varied independently between well-defined limits. Therefore, throughout this paper we will use γ_{cat} and p_2 as the preferred set of input variables. The transformations, regardless of which species is limiting, can be written as

$$\gamma_1 = \gamma_{cat}\,\gamma_{O,\max}(1 - p_2)\max\left[\frac{n_O u_O}{n_{CO}u_{CO}}, 1\right]$$
$$\gamma_2 = \gamma_{cat}\,\gamma_{O,\max}\,p_2 \tag{10}$$

The form of fluxes can also be written, in terms of these two parameters, as

$$\Gamma_O = \gamma_{cat}\,\gamma_{O,\max} n_O u_O, \qquad \Gamma_{CO} = (1 - p_2)\Gamma_O$$
$$\Gamma_{CO_2} = \Gamma_{CO}, \qquad \Gamma_{O_2} = \tfrac{1}{2} p_2 \Gamma_O \tag{11}$$

The preceding equation set can be used to model wall catalycity without being limited by the assumption of a particular site balance reaction model. The drawback of this approach is that γ_{cat} and p_2 remain as unknown parameters with unknown dependencies on factors like temperature, densities, surface condition, etc. Such dependencies can somewhat be described by an appropriate surface site balance model, however, the validity of such models, especially the commonly used ER model, is unknown. Therefore, in this work we will deal with γ_{cat} and p_2 that have clear physical interpretations and that can be varied independently between well-defined limits. Note that the limiting case of the supercatalytic wall cannot be modeled directly via this parameterization because the supercatalytic wall model does not account for rate limiting nor elemental separation in the boundary layer due to unequal species diffusion coefficients. However, the maximum heat flux predicted by the current model will approach the supercatalytic limit as long as the surface reactions are diffusion (rather than rate) limited.

E. Heat Flux Variation due to Wall Catalytic Parameters

We now present the variation of peak stagnation point heat flux with the catalytic parameters γ_{cat} and p_2 defined in the last section. Figure 3a shows the variation of the stagnation point heat flux with

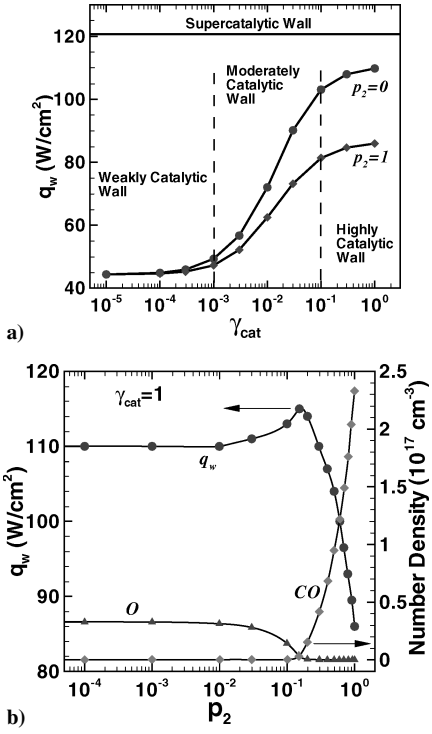

Fig. 3 Impact of catalytic modeling parameters: a) effect of varying catalytic efficiency and preference factor on stagnation heating, and b) effect of varying preference factor $\gamma_{cat} = 1$ on heat flux and wall number densities of gas phase CO and O.

catalytic efficiency, γ_{cat} at two extremes of p_2. The curves in Fig. 3a show a distinct S pattern that defines three distinct regimes of heat flux sensitivity to catalycity. The first is the high catalytic efficiency region ($\gamma_{cat} > 0.1$), where the heat flux weakly varies with the value of γ_{cat} because the recombination rate is limited by the transport (diffusion) of reactants (CO and O) through the boundary layer to the wall. An important consequence of the diffusion-limiting phenomenon is that for heat shield design, it is not critical to know that exact value of catalytic efficiency γ_{cat} as long as it is confirmed that the catalytic efficiency is high. Note, however, that even in the diffusion-limited regime a precise determination of the preference factor p_2 may still be necessary, as seen by the large difference between the $p_2 = 0$ and 1 heat flux levels in Fig. 3a. This will be further discussed later in this section. The second region in Fig. 3a is the moderate catalytic efficiency regime ($10^{-3} < \gamma_{cat} < 10^{-1}$). In this regime, the heat flux is highly sensitive to the exact value of γ_{cat} because the recombination rate is surface process rate limited. In this regime, a precise determinations of γ_{cat} and p_2 are essential for heat flux computation. The third region in Fig. 3a is the weakly catalytic regime ($\gamma_{cat} < 10^{-3}$), where, again, the exact value of γ_{cat} is unimportant to heating because wall catalycity contributes little to the heating as compared to thermal conduction from the hot gas. These three catalytic regimes will be frequently referred to throughout this paper because the sensitivity and uncertainty analyses are performed separately for each of these regimes.

Figure 3b shows the variation of the stagnation point heat flux q_w vs the preference factor p_2, assuming a fully catalytic wall ($\gamma_{cat} = 1$). The parameter p_2 represents the importance of $O + O \rightarrow O_2$ channel as compared to $CO + O \rightarrow CO_2$ reaction channel. Note that although CO oxidation by adsorbed O atoms has been well studied on transition state metals for catalytic converter applications, CO + O recombination was found not to occur at detectable levels on quartz surfaces analyzed by Sepka et al.[22] and Kolesnikov et al.[23] However, O + O recombination was detected in the presence of CO on these surfaces in both investigations. This raises the question as to whether CO + O recombination is likely to occur in flight where the surface temperature is well above 1000 K. In this work, we treat this as a parametric uncertainty by varying p_2. In addition to q_w, Fig. 3b also shows the gas-phase number densities of CO and O at the stagnation point. When p_2 is low, CO + O recombination is dominant, and both CO and O are efficiently utilized. This efficient utilization of both species occurs because the shock-layer number densities of these species are similar in magnitude (because they are produced in equal amounts by direct dissociation of CO_2), which is appropriate for the 1:1 stoichiometric ratio required for CO + O recombination. Figure 3b shows that a slight excess of O atoms (caused due to a faster diffusion of lighter O atoms compared to CO) is seen. The extra O atoms can be further utilized if a small amount of O + O recombination is allowed to occur by raising p_2. This trend is evident in Fig. 3b as a drop in O density and a further rise of q_w as p_2 is raised from a low value to 10^{-1}. This value of q_w is the most conservative estimate possible using the current catalytic mechanism and represents the maximum utilization of CO and O. Once p_2 is raised above this critical value, the catalytic heating begins to fall sharply. This drop occurs because the stoichiometric requirement of the catalytic reactions no longer matches the available number density ratio of CO and O. As a result, a rise in p_2 is accompanied by an underutilization of CO manifested as a rise in its density. At the extreme of $p_2 = 1$, only O atoms are utilized, and CO molecules are reflected back; consequently, the catalytic heating level is at its minimum while still assuming $\gamma_{cat} = 1$.

To obtain a conservative estimate in design, a supercatalytic wall assumption is often employed.[19] This assumption requires that on diffusion to the wall, the species mass fractions recover the freestream composition, which maximizes the recovery of chemical enthalpy on the surface. For the Mars Pathfinder simulations in this work, the supercatalytic heat flux is about 120 W/cm^2. This value, which is about 5 W/cm^2 higher than the maximum obtained via the catalytic mechanism defined in Sec. II.D, is shown in Fig. 3a as a horizontal line. Although this assumption is a useful design tool because it gives a ceiling for catalytic heating, it may also be unphysical. Because the species mass fractions are imposed at the wall, the net flux of a species may be higher than what is allowed by kinetic theory. [See Eq. (2).] The only limiting phenomenon in a supercatalytic assumption is the diffusion process. Nevertheless, we will consider this limiting case along with high, moderate, and low catalytic regimes due to its prevalent use in the literature.

III. Methodology

A Monte Carlo sensitivity and uncertainty analysis involves statistically varying the input parameters and tracking changes in the output of interest, in this case, the heat flux q_w. The details of the methodology can be found in Ref. 5. However, for the sake of completeness, we briefly outline the steps involved in this work as follows:

1) Input variables that need to be varied are first identified. In an aerothermal CFD analysis the input variables can be categorized as reaction rate parameters, vibration–dissociation coupling parameters, vibrational–translational relaxation times, binary interaction collision integrals for transport property calculations (diffusion, viscosity, and thermal conductivity coefficients), and wall catalycity parameters. Because this work focuses only on laminar, nonblowing convective heating predictions, input parameters that relate to bulk material properties, material response, and turbulence models are not considered. For an eight-species kinetic model, 130 input parameters, as shown in Table 3, are independently varied in this work.

2) Variability limits for these input parameters are chosen that roughly represent their typical uncertainties. The chosen variability limits need not represent the true estimated input uncertainties because they will only be used for sensitivity analysis. We vary each input parameter independently and symmetrically about its baseline value using a Gaussian distribution. The only exceptions are the catalytic parameters γ_{cat} and p_2. These parameters are varied within the variability limits (to be specified based on the catalytic regime) using a uniform distribution on a $\log_{10}$ scale because a baseline or most probable value is not known for these quantities. The models used and the parameters varied are also shown in Table 3.

3) Independent input sets generated by randomly varying the parameters are used to make DPLR runs to obtain corresponding heat flux values. In this work, a total of 3000 axisymmetric runs are made for each catalytic regime to ensure statistical accuracy. Note that the convergence rate of a Monte Carlo simulation is independent of the number of input parameters employed.

4) Input–output correlation coefficients are computed using linear regression analysis, and the fractional contribution of each input variability to the overall output variability is obtained. The largest contributors are the ones that cause the most sensitivity to heat flux. This allows us to short list a handful of the parameters out of the 130 considered.

Table 3 DPLR input parameters to be varied for sensitivity and uncertainty analysis

Input Category	Model	Parameter varied	No. of input parameters	Variability for sensitivity analysis
Dissociation reaction rates	$k = A_M T^{\eta} \exp(-D/T_a)$	A_M	40	±1 order of magnitude
Exchange reaction rates	$k = A\, T^{\eta} \exp(-D/T_a)$	A	7	±1 order of magnitude
Vibration–dissociation coupling	$T_a = T^{\eta} T_V^{1-\eta}$	η	5	±0.15
V–T relaxation time	Millikan and White[9]/Camac[10]	Slope	40	±10%
Binary collision integral	$\Omega^{1,1}, \Omega^{2,2} = A\, f(T)$	A	36	±30%
Wall catalysis	See text	$\gamma_{cat}\, p_2$	2	Entire range

5) For the short listed input parameters, a more accurate estimate of their associated uncertainties is performed.

6) A second set of calculations is then made. For this run, the variability of the short listed parameters is adjusted according to their estimated uncertainties, whereas all other parameters are varied according to the initial estimates. The variability in the output now represents the parametric uncertainty. The input–output correlations are again computed to apportion the output uncertainty into those of input parameters.

Note that the chosen input uncertainties in step 2 must at least bound the expected value because the magnitude of the resulting sensitivity will be directly related to the magnitude of the input uncertainty. The penalty for overestimating the magnitude of some uncertainties in step 2 is (at worst) an increase in the number of short listed input parameters for which accurate uncertainties must be determined. However, if one or more input uncertainties are severely underestimated, they may be erroneously ignored as significant contributors to the overall output uncertainty.

IV. Sensitivity Analysis

In the remainder of this paper the sensitivity and uncertainty analysis results are presented separately for each of the catalytic regimes mentioned in the preceding sections. This partitioning is performed because the sensitivities and the rate-limiting steps at play in these regimes are significantly different in each catalytic regime. In the next four subsections we present sensitivity analysis results for the stagnation point of the Mars Pathfinder vehicle at the peak heating point on the trajectory. Results at different locations on the surface and different points along the trajectory will be presented in later sections. The sensitivity results are presented as bar charts (Fig. 4), with the bar heights representing the square of the correlation coefficient of each input parameter with the stagnation point heat flux q_w.

A. Supercatalytic Wall

Figure 4a shows that in the supercatalytic case, out of 130 input parameters listed in Table 3, the stagnation point heat flux shows sensitivity to only four parameters. All four are binary collision integrals as labeled in Fig. 4a. Note that, under the assumption of a supercatalytic wall, the catalytic properties γ_{cat} and p_2 do not have any variability. The rate of CO_2 production at the wall is limited only by the diffusion transport of the reactants O and CO (and to a lesser extent O_2) through the boundary layer. However, the near-wall region of the boundary layer in the steady state comprises mostly CO_2 due to the forced surface recombination. Therefore, the diffusion of O and CO in a background of CO_2 are the two major rate limiting processes, as shown by high correlation of the CO_2–O and CO_2–CO binary collision integrals to q_w. Because the boundary layer a small distance away from the wall also comprises CO and O in addition to CO_2, the CO–O interaction also plays a role in determining the diffusion of these species toward the wall. The heat flux also shows slight sensitivity to the CO_2–CO_2 interaction. This collision integral does not affect the catalytic component of heating (self-diffusion plays no role in mass transport), but it does control the thermal conductivity of the near-wall region and, thus, affects the convective component. The heat flux does not show much sensitivity to the gas-phase reaction rates over the range of variability considered in Table 3. The reason for this insensitivity is that the freestream CO_2 is almost completely dissociated after the shock. The CO formed therein remains undissociated throughout the shock and the boundary layer. As a result, not much is different, as far as the major species densities are concerned, when the gas-phase reaction rate constants are varied randomly over an order of magnitude.

B. Highly Catalytic Wall

In this regime we vary γ_{cat} between 10^{-1} and 10^{0}, and p_2 is varied over the range from 10^{-4} to 10^{0} using a uniform distribution on a $\log_{10}$ scale. All other parameters are varied according to a Gaussian distribution. Figure 4b shows the sensitivity of heat flux on various parameters in the highly catalytic regime. In this regime, both transport properties and catalytic parameters show significant correlation with the heat flux, suggesting that this regime is characterized by regions of both diffusion and surface reaction rate limiting. In a significant region of the window of variability, the CO + O surface reaction is CO flux limited, hence, the diffusion of CO in a background of CO_2 gas is one of the rate-limiting steps. Other collisional

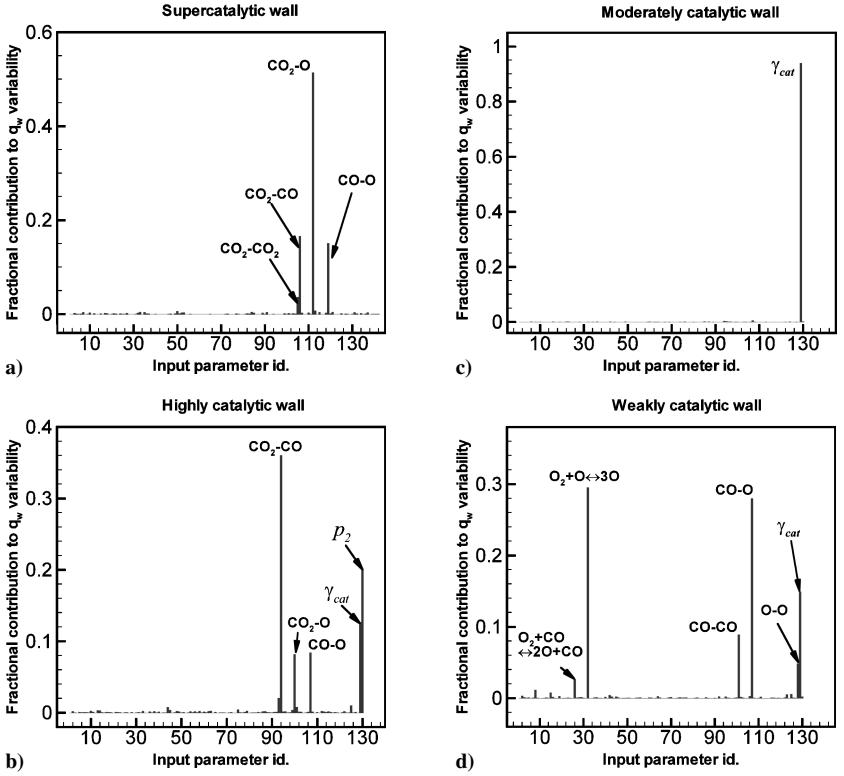

Fig. 4 Fractional contributions to heat flux variability from each input parameter: a) supercatalytic, b) highly catalytic, c) moderately catalytic, and d) weakly catalytic wall; binary collision integrals are labeled as species pairs.

interactions such as CO_2–O and CO–O are also somewhat important because in the window of variability, O flux limiting also occurs, as seen in Fig. 3b. As far as the catalycity parameters are concerned, both γ_{cat} and p_2 also control the heat flux, although the effect of γ_{cat} is somewhat muted because diffusion limiting is slightly more important. However, even in a completely diffusion-limited regime, the effect of p_2 is still large. This effect, as discussed earlier, is due to the efficiency of utilization of CO and O radicals in the catalytic process. If p_2 is large, most of the CO remains unused, and the heat flux is low. On the other hand, if p_2 is small, the heating approaches its maximum due to efficient reactant utilization, although some excess O atoms are left after CO + O recombination is complete.

C. Moderately Catalytic Wall

As shown earlier in Fig. 3a, in the moderate catalytic regime, $10^{-3} < \gamma_{cat} < 10^{-1}$, the heat flux varies very strongly with the value of γ_{cat}, which is also seen in Fig. 4c. This dependence is because surface recombination is no longer limited by diffusion; instead the kinetic rate γ_{cat} controls the recombination. The preference parameter p_2 is less important because a full utilization of reactants CO and O does not occur in this regime. As a result, stoichiometric requirements are not as stringent. Also note that because p_2 was chosen using a uniform distribution on the log scale, the low values of p_2 ($<10^{-1}$) are emphasized. As a result, the weighting on the most sensitive part of the q_w vs p_2 curve ($p_2 > 10^{-1}$) is relatively small. If a uniform distribution of p_2 on a linear scale were chosen, p_2 would appear as a more sensitive quantity. However, because the actual value and variation of p_2 are unknown at this time, either choice is acceptable as long as it is clearly stated.

D. Weakly Catalytic Wall

In this regime, $\gamma_{cat} < 10^{-3}$, the effect of catalycity on heating is low. Instead, the heat flux is determined primarily by thermal conduction from the hot gas. As a result, Fig. 4d shows γ_{cat} as a parameter of secondary importance. The transport properties of CO and O in a gas mixture of CO + O are important because these interactions determine the thermal conductivity of the boundary layer, which comprises mostly CO and O. (CO_2 is absent in the boundary layer due to insignificant recombination.) However, the largest sensitivity of heat flux comes from the $O_2 + O \Leftrightarrow 2O + O$ gas-phase reaction. In the boundary layer, this reaction proceeds in the backward (exothermic recombination) direction. The faster this reaction proceeds, more heated the boundary layer gets, which results in more thermal conduction into the wall. A slight importance of the gas-phase reaction $O_2 + CO \Leftrightarrow 2O + CO$ is because CO is also a dominant species in the boundary layer, although its rate is much smaller than that of the $O_2 + O \Leftrightarrow 2O + O$ reaction.

V. Input Parameter Uncertainty Estimates

A. Transport Properties

As discussed earlier, the transport properties of the gas mixture, including viscosity, thermal conductivity, and binary diffusion coefficients, are computed from binary collision integral data using standard mixing rules. Collision integrals for the 36 binary interactions that occur in an eight-species CO_2–N_2 mixture were taken from the recommendations in Refs. 16 and 17. These data were collected from a variety of sources with varying accuracy. The estimated uncertainties of all 36 interactions were also reported in Refs. 16 and 17; these values are employed in this work. Table 4 lists the uncertainties of the key binary interactions identified in the preceding section.

Table 4 Estimated collision integral uncertainties for key binary interactions

Interaction	Uncertainty, %
CO_2–CO_2	±20
CO_2–CO	±20
CO_2–O	±30
CO–O	±30
CO–CO	±20
O–O	±5

In addition to uncertainties in the component binary interactions, additional uncertainty arises in the mixture transport properties due to nonideal effects such as the mixture rule inaccuracies, the presence of excited state species, and nonequilibrium (non-Boltzmann) distribution of vibrational states. Therefore, an additional 10% uncertainty is added to all collision integrals to account for these nonideal effects. In this work, we assume the same percentage uncertainties for both the Ω^{11} and Ω^{22} collision integrals. This assumption is justified because the ratio of these collision integrals remains near constant.[16,17]

B. Chemical Kinetics

Out of 12 reactions considered in this mechanism, sensitivity analysis shows that only the $O_2 + M \Leftrightarrow 2O + M$ ($M = O$ and CO) reaction shows any sensitivity in laminar convective heating as seen in Fig. 4d. Also, this reaction occurs in the boundary layer in the reverse direction. In this work, we assume that the uncertainty in the forward rate constant is same as that in the backward rate. The forward rate constant for this reaction was recommended by Park[24] after reinterpretation of shock-tube data using a two-temperature model. However, most of the experimental data points were at temperatures higher than the typical boundary-layer temperature of 1500–2500 K. Although the general agreement with the experimental data is within an order of magnitude, we conservatively assign an order of magnitude uncertainty (95% confidence limit) at lower temperatures typical in the boundary layer.

VI. Uncertainty Analysis

In this section, we present the uncertainty analysis data for the four catalytic regimes, again at the stagnation point of the vehicle at the peak heating point of the entry trajectory. For each case, we show a probability distribution of the stagnation point heat flux showing its uncertainty and its apportionment to the input parameter uncertainties. All input parameters that contribute less than 5% to the heat flux uncertainty are lumped into a single other category. Also note that the apportionment of the heat flux uncertainty into input uncertainties assumes a near linear behavior of the model; possible interaction effects are neglected in the linear regression analysis performed.

A. Supercatalytic Wall

The uncertainty due to the catalysis model is eliminated by employing a conservative supercatalytic wall assumption. Although this assumption gives the upper ceiling of the catalytic heat flux, the ceiling itself is uncertain due to uncertainties in other input parameters. Figure 5a shows the probability distribution of the heat flux for this case. The 95% confidence limits are found to be 120.6 W/cm^2 (+10.3%, −9.9%) at the stagnation point. The possibility that the supercatalytic heat flux can be larger by an additional 10.3% (of course, with decreasing probability) has important design and risk mitigation consequences. Figure 5b shows the apportionment of the heat flux uncertainty. As seen during the sensitivity analysis, CO_2–O collision interaction is the largest source of uncertainty to the heat flux because this parameter controls the diffusion-limited catalytic recombination rate. This is followed by other lesser important collisional interactions: CO–O and CO_2–CO. About 13% of the uncertainty is contributed by the rest of the parameters combined.

B. Highly Catalytic Wall

In the highly catalytic regime, the surface recombination processes approach diffusion limiting, which is apparent from a large contribution (32%) to the heating uncertainty from the CO_2–CO collision integrals. However, finite rate catalycity is still a significant contributor to heat flux uncertainty. As we mentioned earlier, at high catalycity, p_2, the preference factor plays a crucial role in determining the net heat flux and consequently appears as one of the larger contributors to the uncertainty. It was also shown in Fig. 3b that most of the variability in p_2 caused the heat flux to remain at

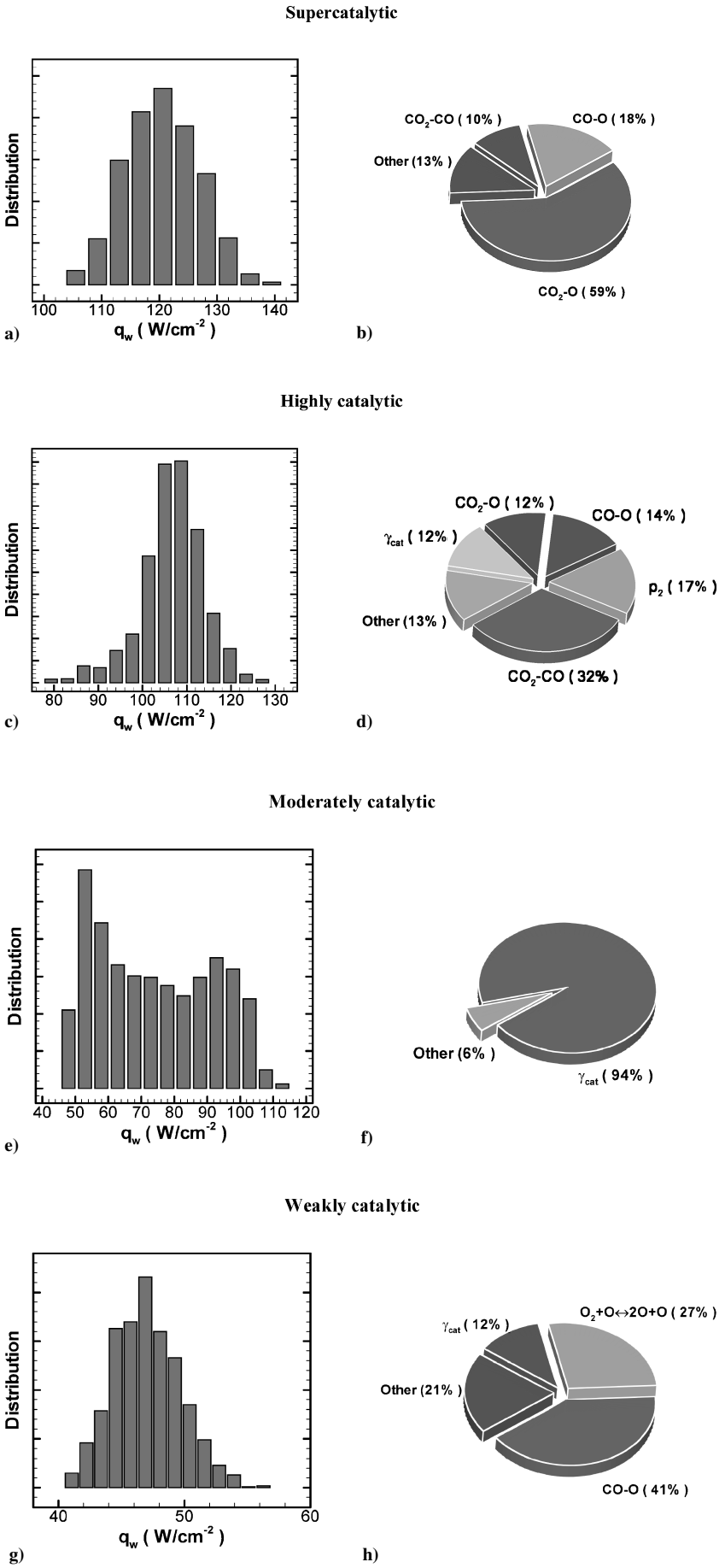

Fig. 5 Stagnation point heat flux probability distributions and uncertainty contributions: a–b) supercatalytic, c–d) highly catalytic, e–f) moderately catalytic, and g–h) weakly catalytic wall.

higher values, close to the maximum, except when p_2 is high when the heat flux rapidly drops. This causes an asymmetric probability distribution of heat flux with the peak of the distribution near the higher value as seen in Fig. 5c. The catalycity parameter γ_{cat} also contributes a 12% uncertainty because of surface process limiting at the lower end of catalycity within the confines of this regime. The 95% confidence limits for the stagnation point heat flux are 106.7 W/cm^2 (+12.0%, −17.2%).

C. Moderately Catalytic Wall

The uncertainty in the moderately catalytic regime, $10^{-3} < \gamma_{cat} < 10^{-1}$, is dominated by the uncertainty in the value of γ_{cat}, which in this case is uniformly distributed over the entire range (in log scale). The catalytic recombination in this regime is surface process rate limited. The distribution of the heat flux in Fig. 5e is much different from a Gaussian that is seen in other regimes. The reason for a relatively broad distribution is that the dominant input γ_{cat} is not varied according to a Gaussian distribution. Moreover, the heat flux distribution function is skewed toward the lower values. This effect occurs due to the variations caused by p_2, the preference factor. As seen in Fig 3b, in the lower end of the moderately catalytic regime, $\gamma_{cat} \sim 10^{-3}$, the effect of p_2 on heat flux is very small, which allows the heat flux values to be concentrated near the lower limit value. On the other hand, a strong effect of p_2 is observed at the higher end of this regime, $\gamma_{cat} \sim 10^{-1}$, due to reasons discussed earlier, which consequently causes spreading of heat flux to lower values. The 95% confidence limits for the stagnation point heat flux in this regime are 74.0 W/cm^2 (+41.0%, −33.6%). Figure 5f shows that most of the heat flux uncertainty is due to γ_{cat}.

D. Weakly Catalytic Wall

In the weakly catalytic regime, $\gamma_{cat} < 10^{-3}$, the heat flux is dominated by conduction effects, which are controlled by the boundary-layer temperature and the thermal conduction due to collisional interaction of the dominant species. Because the near-wall boundary-layer composition in a weakly catalytic regime is mostly CO and O, the uncertainty in the CO–O collision integral appears as the largest contributor (Fig. 5h) to the heating uncertainty via thermal conductivity changes. The $O_2 + O \Leftrightarrow 2O + O$ reaction is the dominant recombination reaction in the boundary layer. This reaction results in a rise of boundary-layer temperature and, consequently, a larger heat flux. The catalytic parameter γ_{cat} also contributes about 12% to the uncertainty, indicating that catalytic heating is still present. The overall spread of the heat flux distribution in Fig. 5g, however, is much smaller in this regime with the 95% confidence limits being 47.2 W/cm^2 (+11.7%, −10.6%).

VII. Uncertainty in Distributed Heating

The findings of the uncertainty analysis at the peak heating point on the trajectory are summarized in Fig. 6. The heat flux uncertainty is largest in the moderately catalytic condition due to a high sensitivity to γ_{cat}, which is a source of large uncertainty. In the highly catalytic regime, the heat flux uncertainty is reduced due to diffusion limiting. Under highly catalytic and supercatalytic conditions, the heat flux uncertainties are dominated by diffusion coefficient uncertainties, which, in general, contribute less to the heating uncertainty. In the highly catalytic regime, the preference parameter p_2 that controls the utilization of CO and O at the wall, is also a contributor to the uncertainty. The smallest heat flux uncertainty is found in the weakly catalytic regime because the thermal conductivity and boundary-layer temperature uncertainties are relatively lower, and the catalytic uncertainty contributes very little by definition. Figure 6 also shows heating uncertainties at midfrustum and shoulder points in the forebody. The numerical uncertainty results at all three body points examined in this paper are summarized in Table 5. Although the magnitude of the heat flux is smaller at the midfrustum and shoulder points, the trends in and magnitudes of the total uncertainty in heat flux across the different catalytic regimes are consistent at all body points.

Table 5 Heating results at peak heating trajectory point

Body location	q_w, W/cm^2	95% confidence limits (±), %	
	Supercatalytic		
Stag. point	120.6	+10.3	−9.9
Midfrustum	68.7	+12.7	−10.5
Shoulder	72.9	+9.8	−8.1
	Highly catalytic		
Stag. point	106.7	+12.0	−17.2
Midfrustum	61.6	+13.1	−19.2
Shoulder	65.1	+11.1	−18.0
	Moderately catalytic		
Stag. point	74.0	+41.0	−33.6
Midfrustum	46.6	+34.7	−32.5
Shoulder	45.3	+38.6	−30.9
	Weakly catalytic		
Stag. point	47.2	+11.7	−10.6
Midfrustum	30.2	+12.2	−10.8
Shoulder	30.4	+9.0	−8.1

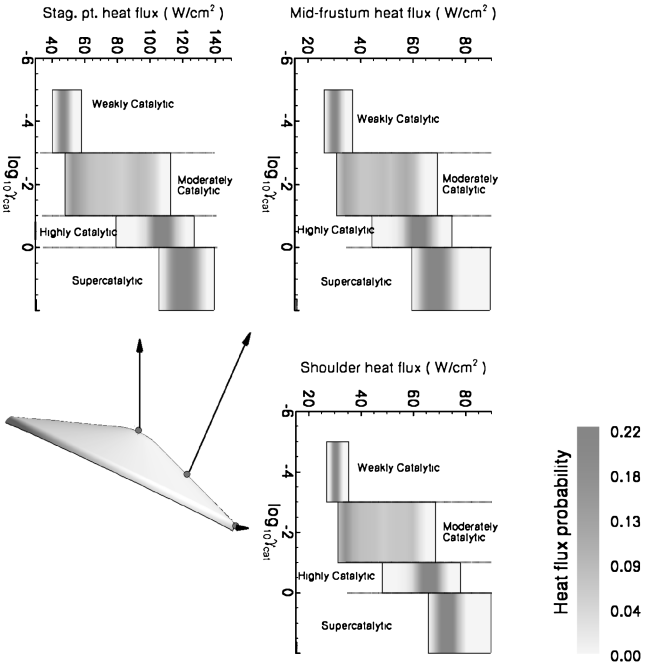

Fig. 6 Stagnation point heat flux probability distribution at peak heating in different catalytic regimes.

VIII. Results at Other Trajectory Points

The uncertainty results presented in the preceding sections were for the peak heating (66-s) trajectory point (Table 1). Uncertainty data were also generated at two other trajectory points to determine if there was a trajectory-dependent element to the results. The same uncertainty process was used for the off-peak heating cases; 3000 DPLR solutions were generated for each catalytic condition with all input variables (except γ_{cat} and p_2) varied according to a Gaussian distribution.

The primary contributors to heat flux uncertainty for the supercatalytic wall cases were examined first. As was the case with the peak heating solutions, the main contributors to the uncertainty at the off-peak heating trajectory points are the collision integrals between CO_2, CO, and O. At all three trajectory points, the CO_2–O collision integral is the largest contributor to the uncertainty. Three primary collision integrals (CO_2–O, CO–O, and CO_2–CO) account for about 90% of the total uncertainty for all three supercatalytic cases.

Trajectory-dependent effects are more pronounced for the highly catalytic wall, as seen in Table 6. Here, γ_{cat} is the largest contributor

Table 6 Uncertainty results comparison for highly catalytic wall

Input variable	$t = 45$ s	$t = 66$ s	$t = 76$ s
γ_{cat}	0.50	0.12	0.02
p_2	Small	0.17	0.54
$\Omega(CO_2\text{–}CO)$	0.16	0.32	Small
$\Omega(CO\text{–}O)$	0.12	0.14	0.10
$\Omega(CO_2\text{–}O)$	0.04	0.12	0.24
$CO + CO \Leftrightarrow CO_2 + C$	0.09	Small	Small
Other	0.09	0.13	0.10

Table 7 Uncertainty results comparison for weakly catalytic wall

Input variable	$t = 45$ s	$t = 66$ s	$t = 76$ s
γ_{cat}	Small	0.12	0.22
Ω (CO–O)	0.54	0.41	0.19
$CO + O \Leftrightarrow C + 2O$	0.20	Small	Small
$O_2 + O \Leftrightarrow 3O$	Small	0.27	0.32
Other	0.26	0.20	0.27

to the heating rate uncertainty at the $t = 45$ s trajectory point, but the effect of γ_{cat} is only 0.12 at the peak heating point and decreases further to 0.02 at the $t = 76$ s trajectory point. Conversely, the effect of p_2 increases as the vehicle travels along the trajectory. The p_2 parameter contributes an insignificant amount to the uncertainty at $t = 45$ s but is the largest component of uncertainty at $t = 76$ s. The differences in what input parameters affect the uncertainty for a highly catalytic wall can be attributed to the changing nature of the flowfield at the different trajectory points. The increased density at $t = 76$ s promotes more gas-phase recombination in the boundary layer compared to the lower density conditions at $t = 45$ s. The higher density drives the flow to a more equilibrium state, in part via the $CO_2 + O \Leftrightarrow O_2 + CO$ reaction. The near wall region at $t = 76$ s is always O-atom deficient due to the amount of recombination into O_2. In addition, the breakpoint between the flow being diffusion or rate limited has been driven to smaller values of γ_{cat} at $t = 76$ s. At $t = 45$ s, there is less tendency toward gas-phase recombination, and the peak efficiency value of p_2 is shifted to larger values closer to one. The recombination of CO_2 and O_2 at the wall is not diffusion limited at $t = 45$ s, meaning that the heating rate will be more sensitive to the value of γ_{cat}.

The uncertainty results for the moderately catalytic wall are consistent at all three trajectory points. The dominant contributor to the uncertainty is γ_{cat}, which accounts for at least 90% of the total uncertainty. This finding is not surprising given that this regime is chosen to encompass that portion of parameter space where the surface catalytic reactions are rate limited (Fig. 3a) and indicates that the bounds of this regime are relatively constant over the trajectory.

The uncertainty results for the weakly catalytic wall at the three trajectory points are shown in Table 7. As was seen in Fig. 3a, at weakly catalytic values of γ_{cat}, the heating rate is insensitive to changes in p_2. Therefore, p_2 is an insignificant contributor to the heating rate uncertainty for all three trajectory points. The importance of γ_{cat} increases with increasing density because catalycity is a larger percentage of the total heating at higher densities. As was discussed earlier, the amount of gas-phase recombination increases with increasing density. At the $t = 45$ s trajectory point where the amount of atomic oxygen is comparatively high and the amount of diatomic oxygen is comparatively low, the CO–O collision integral and $CO + O \Leftrightarrow C + 2O$ reaction make significant contributions to the overall uncertainty. As the gas-phase oxygen recombination increases with increasing density, the uncertainty contributions from these two quantities decreases, and the effect of the $O_2 + O \Leftrightarrow 3O$ reaction kinetics becomes more important.

Finally, Table 8 lists the stagnation point heating and 95%, that is, 2σ, confidence limits, for all three trajectory points at the four catalytic conditions. As was the case at the peak heating point, the

Table 8 Stagnation point uncertainty results at other trajectory points

Time, s	q_w, W/cm$_2$	95% confidence limits (±), %	
	Supercatalytic		
45	55.8	+11.3	−9.0
66	120.6	+10.3	−9.9
76	91.6	+12.3	−10.5
	Highly catalytic		
45	45.7	+13.9	−13.5
66	106.7	+12.0	−17.2
76	77.8	+16.7	−27.9
	Moderately catalytic		
45	28.5	+43.8	−26.8
66	74.0	+41.0	−33.6
76	54.9	+46.7	−39.0
	Weakly catalytic		
45	21.7	+14.1	−11.4
66	47.2	+11.7	−10.6
76	31.5	+12.8	−12.0

off-peak heating solutions show the greatest spread in the heating rate data at the moderately catalytic condition. Again, the reason for this effect is that in the moderately catalytic regime changes to γ_{cat} can have a marked effect on the computed heating rate. Generally speaking, the 95% confidence limit values are greater at the $t = 76$ s trajectory point than they are at the peak heating or $t = 45$ s trajectory points. This result is most pronounced for the highly catalytic wall.

IX. Summary

In summary, a Monte Carlo uncertainty and sensitivity analysis was performed for Mars Pathfinder entry convective aeroheating. The Pathfinder case was selected to be representative of a moderate Mars atmospheric entry condition. A parametric flux-based wall catalysis model was developed that consists of two major recombination channels: $CO + O \rightarrow CO_2$ and $O + O \rightarrow O_2$. Based on the bounds defined by this catalytic model, sensitivity and uncertainty analyses were performed for four different catalytic regimes, namely, supercatalytic, highly catalytic, moderately catalytic, and weakly catalytic walls.

The sensitivity analysis found that, for supercatalytic and highly catalytic regimes, the binary collision integrals are the most critical input parameters due to diffusion rate limiting. The reaction preference factor p_2 also appears as a vital input parameter at high catalycity. For moderate catalycity, a high sensitivity of heat flux to the catalytic parameter γ_{cat} implies heterogeneous reaction rate limiting. In the weakly catalytic regime, the thermal conduction, determined by the binary collision integrals and the $O + O$ gas-phase recombination rates, appear as the most important parameters. There was some trajectory-dependent behavior to the uncertainty results that was evident when calculations were performed at two off-peak heating points in the trajectory. The changes in the uncertainty contributions were due to differences in gas-phase recombination, peak efficiency value of p_2, and reaction kinetics caused by differences in boundary-layer density at the different trajectory points.

The findings of this study indicate that improved characterization of the catalytic properties of thermal protection material surfaces under flight conditions will result in a significantly improved heat flux prediction and, consequently, in a reduced heatshield margin, a lower TPS mass, or a wider choice of materials. Even for the most conservative supercatalytic wall model an additional 10% uncertainty must be carried to account for other input modeling parameters. If the surfaces are deemed highly catalytic, which is often assumed due to surface roughness or formation of an ablative char layer, a more precise determination of the key binary collision integrals and an improved diffusion model will yield maximum improvement in laminar real gas Navier–Stokes aeroheating predictions.

Acknowledgments

This work was funded by the In-Space Propulsion program under Task Agreement M-ISP-03-18 to NASA Ames Research Center. The work performed by Deepak Bose and Grant Palmer was supported by the Prime Contract NNA04BC25C to Eloret Corporation. We would also like to thank Y.-K. Chen, Nagi Mansour, and James Brown of NASA Ames Research Center for suggesting manuscript improvements.

References

[1]Johnson, L., Alexander, L., Bagett, R., Bonometti, J., Hermann, M., James, B., and Montgomery, S., "NASA's In-Space Propulsion Program: Overview and Update," AIAA Paper 2004-3841, July 2004.

[2]Chen, Y.-K., Henline, W. D., and Tauber, M. E., "Mars Pathfinder Trajectory-Based Heating and Ablation Calculations," *Journal of Spacecraft and Rockets*, Vol. 32, No. 2, 1995, pp. 225–230.

[3]Mitcheltree, R. A., and Gnoffo, P. A., "Wake Flow About the Mars Pathfinder Entry Vehicle," *Journal of Spacecraft and Rockets*, Vol. 32, No. 5, 1995, pp. 771–776.

[4]Milos, F. S., Chen, Y.-K., Congdon, W. M., and Thornton, J. M., "Mars Pathfinder Entry Temperature Data, Aerothermal Heating, and Heatshield Material Response," *Journal of Spacecraft and Rockets*, Vol. 36, No. 3, 1999, pp. 380–391.

[5]Bose, D., Wright, M. J., and Gökçen, T., "Uncertainty and Sensitivity Analysis of Thermochemical Modeling for Titan Atmospheric Entry," AIAA Paper 2004-2455, June 2004.

[6]Spencer, D., Blanchard, R., Braun, R., Kallemeyn, P., and Thurman, S., "Mars Pathfinder Entry, Descent, and Landing Reconstruction," *Journal of Spacecraft and Rockets*, Vol. 36, No. 3, 1999, pp. 357–366.

[7]Wright, M. J., Candler, G. V., and Bose, D., "Data-Parallel Line Relaxation Method for the Navier–Stokes Equations," *AIAA Journal*, Vol. 36, No. 9, 1998, pp. 1603–1609.

[8]Cheatwood, F. M., and Gnoffo, P. A., "User's Manual for the Langley Aerothermodynamic Upwind Relaxation Algorithm (LAURA)," NASA TM 4764, April 1996.

[9]Millikan, R., and White, D., "Systematics of Vibrational Relaxation," *Journal of Chemical Physics*, Vol. 39, No. 12, 1963, pp. 3209–3213.

[10]Camac, M., "CO_2 Relaxation Processes in Shock Waves," *Fundamental Phenomena in Hypersonic Flow*, edited by J. G. Hall, Cornell Univ. Press, New York, 1964, pp. 195–215.

[11]Gurvich, L., Veyts, I., and Alcock, C. (eds.), *Thermodynamic Properties of Individual Substances*, 4th ed., Hemisphere, New York, 1991.

[12]Gupta, R., Yos, J., Thompson, R., and Lee, K., "A Review of Reaction Rates and Thermodynamic and Transport Properties for an 11-Species Air Model for Chemical and Thermal Nonequilibrium Calculations to 30000 K," NASA RP 1232, Aug. 1990.

[13]Palmer, G. E., and Wright, M. J., "A Comparison of Methods to Compute High-Temperature Gas Viscosity," *Journal of Thermophysics and Heat Transfer*, Vol. 17, No. 2, 2003, pp. 232–239.

[14]Palmer, G. E., and Wright, M. J., "A Comparison of Methods to Compute High Temperature Gas Thermal Conductivity," AIAA Paper 2003-3913, June 2003.

[15]Ramshaw, J. D., "Self-Consistent Effective Binary Diffusion in Multicomponent Gas Mixtures," *Journal of Non-Equilibrium Thermodynamics*, Vol. 15, No. 3, 1990, pp. 295–300.

[16]Wright, M. J., Hwang, H. H., and Schwenke, D. W., "Recommended Collision Integrals for Transport Property Computations II: Mars and Venus Entries," *AIAA Journal* (submitted for publication).

[17]Wright, M. J., Bose, D., Palmer, G. E., and Levin, E., "Recommended Collision Integrals for Transport Property Computations I: Air Species," *AIAA Journal*, Vol. 43, No. 12, 2005, pp. 2558–2564.

[18]Park, C., Howe, J. T., Jaffe, R. L., and Candler, G. V., "Review of Chemical-Kinetic Problems of Future NASA Missions, II: Mars Entries," *Journal of Thermophysics and Heat Transfer*, Vol. 8, No. 1, 1994, pp. 9–23.

[19]Wright, M. J., Olejniczak, J., Brown, J. L., Hornung, H., and Edquist, K. T., "Computational Modeling of T5 Laminar and Turbulent Heating on Blunt Cones, Part 2: Mars Applications," AIAA Paper 2004-2455, June 2004.

[20]Christmann, K., *Introduction to Surface Physical Chemistry*, Springer-Verlag, New York, 1991, pp. 203–206.

[21]Chen, Y.-K., Henline, W. D., Stewart, D. A., and Candler, G.V., "Navier–Stokes Solutions with Surface Catalysis for Martian Atmospheric Entry," *Journal of Thermophysics and Heat Transfer*, Vol. 30, No. 1, 1993, pp. 32–42.

[22]Sepka, S., Chen, Y.-K., Copeland, R., and Marschall, J., "Experimental Investigations of Surface Reactions in Carbon Monoxide and Oxygen Mixtures," *Journal of Thermophysics and Heat Transfer*, Vol. 14, No. 1, 2000, pp. 45–52.

[23]Kolesnikov, A., Yakushin, M., Pershin, I., and Vasilevskii, S., "Heat Transfer Simulation and Surface Catalycity Prediction at the Martian Atmosphere Entry Conditions," AIAA Paper 99-4892, July 1999.

[24]Park, C., "Two-Temperature Interpretation of Dissociation Rate Data for N_2 and O_2," AIAA Paper 88-0458, Jan. 1988.